



# Three in one: One host–guest doping system with mechanochromism, long afterglow, and thermally activated delayed fluorescence

Chao Yang<sup>a,1</sup>, Meiling Pan<sup>b,2</sup>, Lei Ma<sup>b,3</sup>, Yongtao Wang<sup>a,4</sup>

<sup>a</sup> College of Chemistry and Bioengineering, Guilin University of Technology, Guilin 541004, China

<sup>b</sup> Tianjin International Center for Nanoparticles and Nanosystem, Tianjin University, Tianjin 300072, China

## ARTICLE INFO

### Keywords:

Mechanochromism  
Thermally activated delayed fluorescence  
Host-guest doping  
Long afterglow  
Encryption

## ABSTRACT

Multifunctional luminogens with dual-state emission, mechanochromism, acidichromism, and multi-color long afterglow are very popular, especially in the fields of anti-counterfeiting and information encryption. However, achieving thermally activated delayed fluorescence (TADF) type multi-color long afterglow and mechanochromism with lifetime dimension and “switch-on” fluorescence response still face great challenges due to unpredictable intermolecular interactions and molecular conformation, weak intersystem crossing between singlet and triplet states, and easily deactivated triplet excitons. Here, a multifunctional luminogen named as 4-(4'-(diphenylamino)-[1,1'-biphenyl]-4-yl)-2,6-dimethylpyridine-3,5-dicarbonitrile (DBdD) was designed and synthesized, showing solvatochromism, dual state emission, phosphorescence nature, acidichromism, “switch-on” type and morphology dependent mechanochromism. In binary and ternary host–guest doping systems of DBdD, multi-color long afterglow coming from TADF and Förster resonant energy transfer (FRET), as well as mechanochromism with lifetime dimension were achieved in sequence. Based on the above acidichromism, different afterglow lifetimes, and multi-color long afterglow, DBdD and its doping systems showed potential applications in advanced information encryption and anti-counterfeiting. More importantly, this work will provide valuable insights into the mechanisms governing “switch-on” type mechanochromism and TADF type long afterglow.

## 1. Introduction

Luminogens absorb photons via photoexcitation and transition to a higher excited state energy level, then back to the ground state and emit photons after the relaxation process, which is called as photoluminescence [1–6]. Photoluminescence can be divided into fluorescence, phosphorescence, and TADF according to different transitions and intersystem crossing (ISC) processes. Owing to aggregation caused fluorescence quenching, most of the luminogens cannot produce dual-state fluorescence emission in solution and aggregated state, which is not conducive to expanding their application scopes and reducing application costs. By conjugation induced rigidity and space conjugation in the twisting molecule, some organic luminogens with dual state emission property were achieved [7–12]. Even so, molecule design strategy and mechanism of dual-state emission are not still well-established. Compared with traditional fluorescence luminogens, pure organic long afterglow materials show more important application value in bioimag-

ing, information encryption, oxygen sensing, and chirality recognition due to long duration and large Stokes shifts. But organic long afterglow materials often suffer from weak spin–orbit coupling between singlet states and triplet states, as well as sensitive triplet excitons to oxygen and molecular motions, affecting further improvement of afterglow lifetime and brightness. In theory, TADF materials also involve ISC and triplet excitons, but most of the reported organic long afterglow materials come from room temperature phosphorescence (RTP) [13,14] rather than TADF luminogens because of tiny energy gap ( $\Delta E_{ST}$ ) ( $\leq 0.2$  eV) between the lowest excited singlet state ( $S_1$ ) and the lowest excited triplet state ( $T_1$ ) [15–22], which accelerates reverse intersystem crossing rates ( $k_{RISC}$ ) and contributes to the shortened afterglow lifetimes [23–29]. It is worth highlighting that the development of TADF-based organic afterglow materials heavily relies on the construction of host–guest doping systems, which is also highly appealing. Considering that urea, benzoic acid, methoxybenzophenone, phenyl benzoate,  $\beta$ -estradiol, boric acid, and triphenylphosphine can provide a rigid mi-

E-mail addresses: [lei.ma@tju.edu.cn](mailto:lei.ma@tju.edu.cn) (L. Ma), [wyt\\_shzu@163.com](mailto:wyt_shzu@163.com) (Y. Wang).

<sup>1</sup> <sup>1</sup> Contributed equally

<sup>2</sup> <sup>1</sup> Contributed equally

<sup>3</sup> \* Corresponding authors

<sup>4</sup> \* Corresponding authors

<https://doi.org/10.1016/j.cej.2025.163205>

Received 2 January 2025; Received in revised form 26 April 2025; Accepted 28 April 2025

1385-8947/© 20XX

croenvironment, they were often used as host materials. Unfortunately, most of the host-guest doping systems presented TADF lifetime of 19.2–374.9 ms [15,29–34]. Of note, organic TADF-based afterglow materials with afterglow lifetimes exceeding 566.45 ms and 7 s, respectively, are rare.

Besides, organic long afterglow materials with mechanochromism can provide additional parameters for visual monitoring and are considered an ideal carrier for information storage, encryption, and anti-counterfeiting [35]. However, only a few organic long afterglow materials exhibit mechanochromism by changing molecular conformation, intermolecular stacking and interactions. Yang et al. [36] doped 1,8-naphthalimide into cyanuric acid, resulting in yellow RTP because of the enhanced energy transfer from cyanuric acid to 1,8-naphthalimide after grinding. Ogawa et al [37] reported the first pure organic mechanochromic material with 1,2-diketone molecular skeleton, which was attributed to the phase-transition from crystalline to amorphous state and planarization of molecular conformation. Babu et al. [30] found that intermolecular  $\pi$ - $\pi$  interactions of 1,3,6,8-pyrene tetraborate were promoted after grinding, resulting in the reduced  $\Delta E_{ST}$ , and thereby boosting ISC and achieving efficient RTP. Ma et al. [38] reported a benzophenone derivative with RTP and mechanochromism due to the different molecular conformations of phenothiazine before and after grinding. In 2023, Purkayastha et al. [39] reported two pyrene derivatives with reversible phosphorescent switches by grinding and solvent fumigation. In 2021, Li et al. [40] reported an example with force-induced turn-on persistent RTP. Ma et al. [41] designed a new class of benzoyl derivatives that exhibited reversible phosphorescence conversion under various external stimuli (mechanical force, thermal annealing, and solvent fumes) by molecular packing mode conversion and the alternation of molecular conformation of excited state. Even so, TADF-based organic long afterglow materials with blue shifted and enhanced mechanochromism have not been reported after grinding.

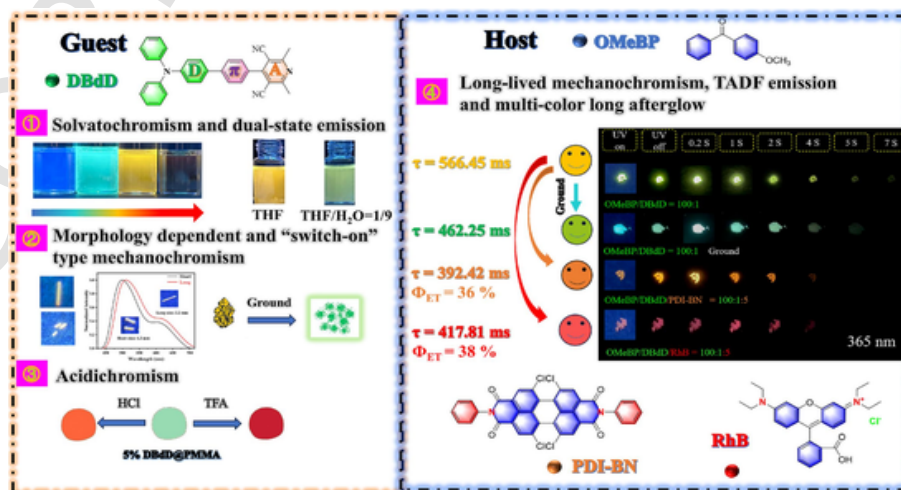
Here, a twisted donor (D)- $\pi$ -acceptor (A) type luminogen (DBdD) was designed and synthesized by using triphenylamine (TPA) and 2,6-dimethyl-3,5-dicyanopyridine (MCP) units as donor and acceptor respectively, whose D and A units were linked by a benzene bridge (Scheme 1). Owing to the large spatial hindrance between MCP unit and benzene bridge, a large twist angle between them was expected to form. Combined with the twisted TPA unit, DBdD should maintain a twisted molecular configuration [8]. Since a rigid structure was essential to constrict intramolecular motion, a planar diphenyl moiety was used as the core to yield high emission in solution [12,21]. On the one side, the twisted D- $\pi$ -A molecular conformation contributed to reducing

$\Delta E_{ST}$  and enhancing the ISC process, leading to TADF or RTP emission. On the other side, dipole-dipole interactions induced by host-guest doping could further tune  $\Delta E_{ST}$  and  $k_{RISC}$ , thereby harvesting TADF emission and afterglow lifetimes over 100 ms. Based on the above mentioned, a series of host-guest doping systems (m% OMeBP/DBdD) were constructed and optimized by choosing DBdD and 4-methoxybenzophenone (OMeBP) as guest and host materials in turn [29], as well as tuning the doping mass ratios (m% was doping mass ratios between DBdD and OMeBP), which presented TADF type long afterglow and mechanochromism with lifetime dimension. Long afterglow materials with red and near-infrared emission need hold a low  $T_1$  energy level, which often increases the nonradiative decay according to the energy gap law, leading to the absence of highly efficient red/NIR RTP [42,43]. On account of FRET theory [44–48], two ternary doping systems named as OMeBP/DBdD/PDI-BN and OMeBP/DBdD/RhB were constructed, whose emission maxima were located at 590 nm and 646 nm in sequence, presenting afterglow lifetimes over 4 s. In addition, crystals DBdD showed “switch-on” type mechanochromism by grinding, while ground DBdD gave morphology dependent mechanochromism by grinding and heating/DCM fuming. More importantly, 1 % OMeBP/DBdD displayed blue shifted and enhanced long-lived TADF type mechanochromism before/after grinding, but not for 1 % OMeBP@PVA film. Furthermore, acidichromism of DBdD and simple recognition of volatile  $\text{CH}_3\text{COOH}$ , HCl, and  $\text{CF}_3\text{COOH}$  were achieved by using DCM solutions, crystal and ground samples, and PMMA doped films of DBdD. Of note, multifunctional DBdD provided convenience for building advanced information encryption and anti-counterfeiting.

## 2. Results and discussion

### 2.1. Solvatochromism and dual state emission

The trace impurities contained in commercial carbazole and triphenylamine significantly enhanced RTP performance of the target compounds [13]. To eliminate the influence of trace impurities, N, N-diphenyl-4-(4,4,5,5-tetramethyl-1,3,2-dioxaborolan-2-yl) aniline (TPAB) was prepared by using diphenylamine as the starting material via C-N coupling and Miyaura boronation reactions. Under the catalysis of acetic acid, 4-bromobenzaldehyde and 3-aminocrotononitrile underwent a cyclization reaction to produce a tetrahydropyridine derivative, which were then oxidized by 2,3-dichloro-5,6-dicyano-1,4-benzoquinone (DDQ) to give 4-(4-bromophenyl)-2,6-dimethylpyridine-



Scheme 1. DBdD main performance diagram.

3,5-dicarbonitrile [6]. Based on Suzuki reaction of TPAB and B, DBdD was successfully prepared (Scheme S1). The  $^1\text{H}$  NMR signal at 2.51 ppm should be ascribed to two methyl groups on the pyridine unit, while the number of residual signals located at 7.05–7.92 ppm matched the number of aromatic hydrogen atoms. Furthermore, the  $^{13}\text{C}$  NMR signals at 24.77 ppm and 107.28–165.06 ppm corresponded to methyl and aromatic rings respectively, and the experimental (499.1892) and calculated values (499.1899) of molecular ion peak ( $[\text{M} + \text{Na}]^+$ ) were consistent. Thereby, DBdD was confirmed by  $^1\text{H}$  NMR,  $^{13}\text{C}$  NMR, HR-MS, and single crystal X-ray diffraction (Fig. S14–S16), whose purity was confirmed by high-performance liquid chromatography (HPLC) (Fig. S17). In various solvents ( $10^{-5}$  M), DBdD had two absorption bands, located at 290–330 nm and 330–440 nm respectively (Fig. 1a) (Fig. S1a), and its emission maxima presented obvious bathochromic shifts (195 nm) with increasing of solvent polarity, indicating strong solvatochromism and intramolecular charge transfer (ICT) effects (Fig. 1b). The relative fluorescence quantum yields ( $\Phi_{\text{RF}}$ ) of the luminogen were determined in various solvents by using quinine sulphate as the refer-

ence (Table S1), whose maximum value was up to 0.50 in toluene, displaying bright single-molecule emission. By tuning water fraction ( $f_w$ ) of THF- $\text{H}_2\text{O}$  solution, aggregation induced emission (AIE) activity of DBdD was examined (Fig. 1c). When  $f_w$  increased to 50 % from 0, emission intensity of DBdD constantly decreased, accompanied by redshifts of emission maxima at  $f_w = 0$ –40 %, and slight blueshifts at  $f_w = 40$ –50 %, which was mainly due to the enhanced ICT effect caused by the increase in solvent polarity (Fig. 1d). Then, emission intensity continuously increased at  $f_w = 60$ –90 % because of the formation of aggregated states, which suppressed molecular motions and the resulting energy loss, corresponding to  $\Phi_{\text{RF}}$  of 0.16 at  $f_w = 90$  %. The formation of aggregated states was verified by the Tyndall phenomenon of THF- $\text{H}_2\text{O}$  solution at  $f_w = 90$  % (Fig. 1c) (Fig. S1f). As expected, DBdD exhibited solvatochromism and dual state emission, with bright fluorescence in THF solution and aggregated states. The dual-state emission phenomenon of DBdD was also observed in dioxane- $\text{H}_2\text{O}$  and DMF- $\text{H}_2\text{O}$  solutions (Fig. S1b–e). Specifically, the  $\Phi_{\text{RF}}$  was 0.40 in diox-

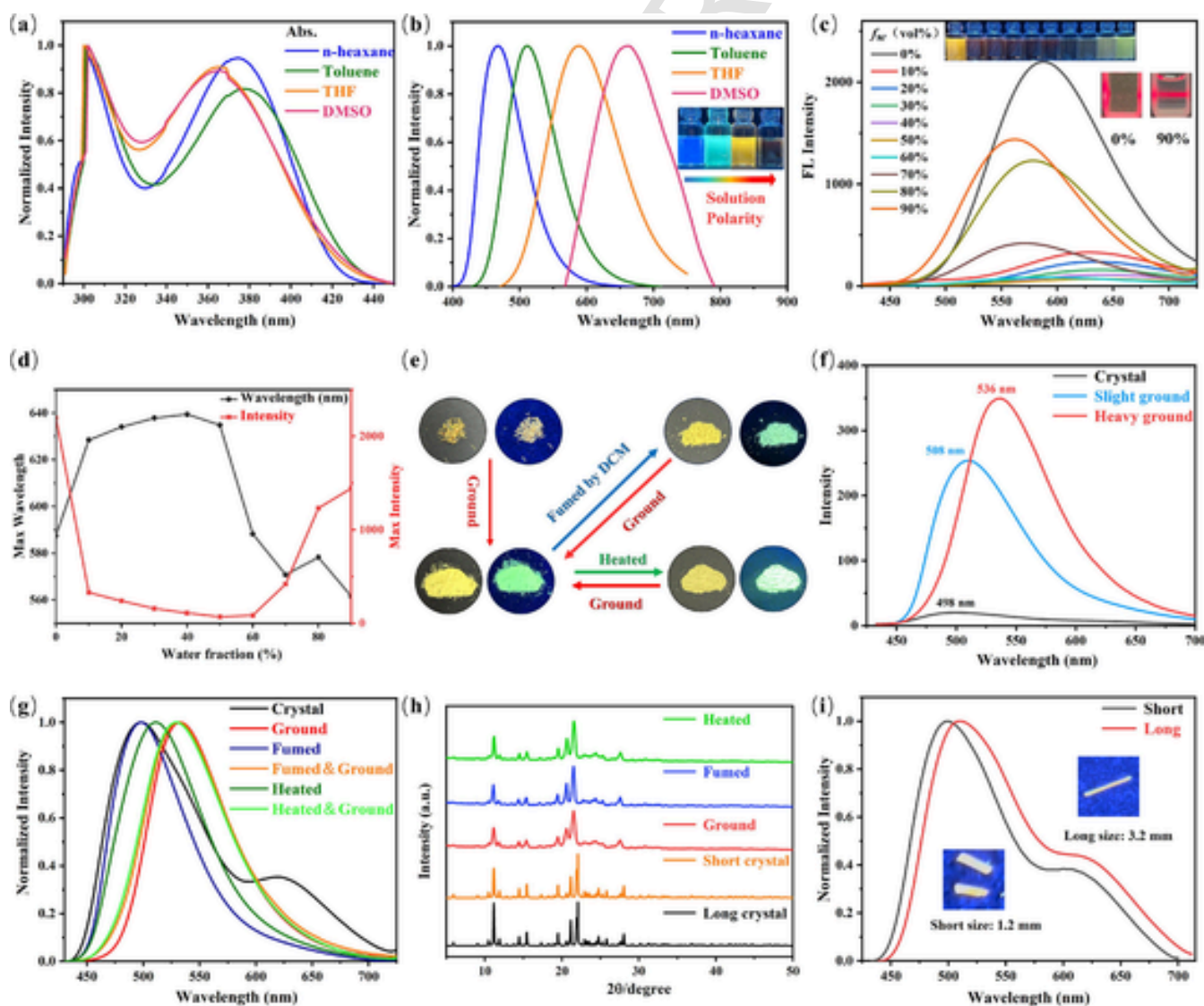


**Fig. 1.** (a) Normalized absorption and (b) fluorescence spectra of DBdD in different solvent ( $10^{-5}$  M) ( $\lambda_{\text{exc}}$ : 372 nm). (c) Fluorescence spectra of DBdD in mixed solvents with different volume ratios of THF/ $\text{H}_2\text{O}$  ( $10^{-5}$  M) ( $\lambda_{\text{exc}}$ : 372 nm) and the Tyndall phenomenon at  $f_w = 90$  %. (d) Chart of the relationship between emission intensity/maxima and water fraction. (e) Photographic images of crystals DBdD before/after grinding, fuming, and DCM fuming under sunlight and 365 nm UV light. (f) Fluorescence spectra of crystals, slight and heavy ground DBdD ( $\lambda_{\text{exc}}$ : 372 nm). (g) Normalized fluorescence spectra of DBdD in different solid states ( $\lambda_{\text{exc}}$ : 372 nm). (h) Powder XRD patterns of DBdD in different sizes and solid states. (i) Normalized morphology-dependent fluorescence spectra of DBdD ( $\lambda_{\text{exc}}$ : 372 nm).

ane and 0.08 in DMF. In the dioxane-H<sub>2</sub>O and DMF-H<sub>2</sub>O solutions at  $f_w = 90\%$ , the  $\Phi_{RF}$  values were 0.14 and 0.38, respectively (Table S1).

By solvent diffusion from n-hexane to DCM solution of DBdD, crystals DBdD were obtained, with yellow appearance under sunlight and 365 nm UV lamp radiation (Fig. 1e). By grinding, DBdD showed high contrast mechanochromism, with bright green fluorescence in UV light. Furthermore, the absolute fluorescence quantum yields ( $\Phi_F$ ) of DBdD were 0.03 and 0.13 before/after grinding respectively (Table S2), corresponding sequentially to 12.43 ns (498 nm), 8.53 ns (618 nm), and 14.51 ns (536 nm) (Fig. S2b-c), displaying “switch-on” type mechanochromism and dual state emission characteristics with fluorescence and RTP (Fig. 1f). RTP characteristics at 618 nm were further confirmed by delay spectrum and time-resolved decay curve (8.53 ns) of crystals DBdD (Fig. S2a, Fig. S2c and Fig. S2f).

## 2.2. Mechanochromism and acidochromism

Of note, ground DBdD samples could not back to their pristine crystal state by heating and DCM fuming, indicating irreversible mechanochromism (Fig. 1g). After grinding, the emission peak at 618 nm disappeared completely, and the emission peak at 498 nm redshifted to 536 nm. Moreover, fumigated and heated DBdD samples showed blue-green and yellow-green fluorescence respectively under UV light radiation (365 nm) (Fig. 1e), corresponding to emission maxima of 498 nm and 510 nm in turn (Fig. 1g). Fumigated and heated DBdD samples were named as Fumed&Ground and Heated&Ground after grinding. Interestingly, Fumed&Ground and Heated&Ground samples presented almost identical fluorescence emission maxima by grinding again. More importantly, fumigated and heated DBdD samples showed reversible mechanochromism by the repeated fuming/heating and grinding, corresponding to emission maxima of 498/510 nm and 536 nm respectively (Fig. S2d-e). To understand the underlying mechanism of mechanochromism, X-ray powder diffractions (XRD) of different solid DBdD samples were investigated. Compared with crystal DBdD samples, XRD signals of ground DBdD samples became wide (Fig. 1h), but the main XRD signals were completely consistent before/after grinding, demonstrating that a small amount of amorphous formation after grinding [49], but ground DBdD still maintained the overall same intermolecular arrangement and stacking modes with crystals DBdD. Furthermore, the formation of a small amount of amorphous state led to increased molecular rotations and vibrations, resulting in red shift of fluorescence emission maxima and the disappearance of the phosphorescence peak at 618 nm. The differential scanning calorimetry (DSC) of DBdD were characterized before/after grinding (Fig. S14b), which showed that the melting temperature of ground DBdD decreased slightly (0.2°C), leading to enhanced intramolecular motions and reduced intermolecular interactions, which also exacerbated the quenching of triplet excitons. More interestingly, ground, heated, and fumigated DBdD gave the same XRD signals (Fig. 1h), but with different emission maxima (Fig. 1g). The reversible mechanochromism of ground, heated, and fumigated DBdD samples should be due to morphology dependent fluorescence emission. The morphology dependent fluorescence emission was further confirmed by carefully selecting crystals of different sizes, and emission maxima of long crystals indicated red shifts of 12 nm compared with that of short crystals (Fig. 1i). For crystals, the long crystals extended the molecular delocalization path, which increased non-radiative energy loss and resulted in red shifts of fluorescence maxima. As further evidence, long and short crystal DBdD samples had the same XRD signals (Fig. 1h), illustrating identical intermolecular arrangements and stacking modes.

The reported literatures showed that some organic molecules with pyridine or quinoline structural unit could exhibit mechanochromism and acidochromism [9,50,51]. It could be inferred from this that the pyridine unit in DBdD was prone to protonation in acidic environment, which would enhance ICT effect and tune intermolecular stacking

mode, leading to wavelength shifts and intensity changes of fluorescence emission. Firstly, a series of acidic DCM solutions of DBdD ( $10^{-5}$  M) were prepared by tuning molar ratios between DBdD and trifluoroacetic acid (TFA)/HCl from 1:1, 1:5, to 1:10. Beyond expectation, the solutions maintained the same absorption and fluorescence maxima (Fig. S3a-b), accompanied by a continuous decrease in fluorescence emission intensity (Fig. S3c-d). <sup>1</sup>H NMR spectra further indicated that DBdD had identical signals before/after adding TFA/HCl (molar ratio of 1:3 between DBdD and TFA/HCl) (Fig. S3e-f) (Fig. S19-20). Thereby, protonation of DBdD was ruled out, which should be attributed to the two electron withdrawing groups (CN) on the pyridine ring reduce the electron donating ability of pyridine. Furthermore, new acidic DCM solutions ( $10^{-5}$  M) of DBdD were prepared by sharply increasing HCl, HOAc, and TFA concentration (adding two drops HCl, HOAc, and TFA per 2 mL DCM solution separately, shaken well, and let it stand for 2 min). The absorption spectra displayed that DCM solution containing HCl (DBdD-HCl) and TFA (DBdD-TFA) yielded new absorption maxima at 490 nm, 531 nm and 758 nm, but without new absorption peak for DCM solution containing HOAc (DBdD-HOAc), indicating that HCl and TFA could interact with DBdD, but not for HOAc (Fig. 2a). Compared with DCM solution of DBdD, absorption maxima of DBdD-TFA solution showed the biggest redshifts (159 nm and 386 nm), followed by DBdD-HCl solution (118 nm), but without obvious redshifts for DBdD-HOAc solution, which were consistent with their fluorescence spectra (Fig. 2b). Obviously, DBdD exhibited different optical properties by tuning the concentration of HCl and TFA in DCM solution, which might come from the formation of complexes between DBdD and HCl/TFA. To understand the intrinsic mechanism of acidochromism, we calculated the binding energy (BE), charge transfer, and charge density difference (CDD) between DBdD and three different acids (HCl, HOAc, TFA). As shown in Table S4, there was no obvious protonation reaction between the three acids and DBdD, which was supposed to be hydrogen bonding interactions between pyridine unit of DBdD and three acids. HOAc showed the lowest BE and charge transfer compared to HCl and TFA, indicating that the interaction of HCl and TFA with DBdD was bigger than that of HOAc, which resulted in DBdD being able to selectively form complex with HCl and TFA rather than HOAc.

Subsequently, crystal and ground DBdD samples were exposed HOAc, HCl and TFA vapors respectively. Fluorescence emission maxima of ground DBdD blue shifted to 527 nm, 519 nm and 512 nm from 536 nm in turn after HOAc (Fig. 2c), HCl and TFA fumigation for three minutes, which maintained constant with the extension of fumigation time for HOAc and HCl (Fig. S4a-b), but with an amazing red shift (734 nm) by extending TFA fumigation time to 10 and 60 min (Fig. S4c). Different from ground DBdD, emission maxima of crystal DBdD at 498 nm gave red shifts of 5 nm after 1 h of HOAc and HCl fumigation, while 618 nm maintained stable (Fig. 2d) (Fig. S4d-e). Interestingly, emission spectra of crystal DBdD yielded significant changes after ten minutes and one hour of TFA fumigation, with single emission maxima at 734 nm (Fig. S4f), indicating better penetration capability for TFA than HCl. After fumigation with different acids, DBdD showed the reduced fluorescence lifetimes, which was consistent with the falling fluorescence emission intensity (Fig. S5a-b). What's more, emission maxima of crystal and ground DBdD samples could recover to their initial states after being placed in a natural environment for one hour (Fig. 2e, Fig. 2f, and Fig. S5d), and no decomposition products were found by thin-layer chromatography detection. Thereby, we believed that DBdD and TFA/HCl could form a complex, resulting in significant changes in absorption and emission spectra. 5 % DBdD@PMMA film was prepared by doping DBdD to PMMA matrix at the mass ratios of 5:100, which was exposed HCl, HOAc, and TFA vapors for 1 min respectively (Fig. S5c). In contrast, 5 % DBdD@PMMA film relative to DBdD solution and ground power showed more significant wavelength shifts, with emission maxima of 625 nm and 732 nm for HCl and TFA fumigation in sequence (Fig. 2g), but with the same emission maxima for the pristine

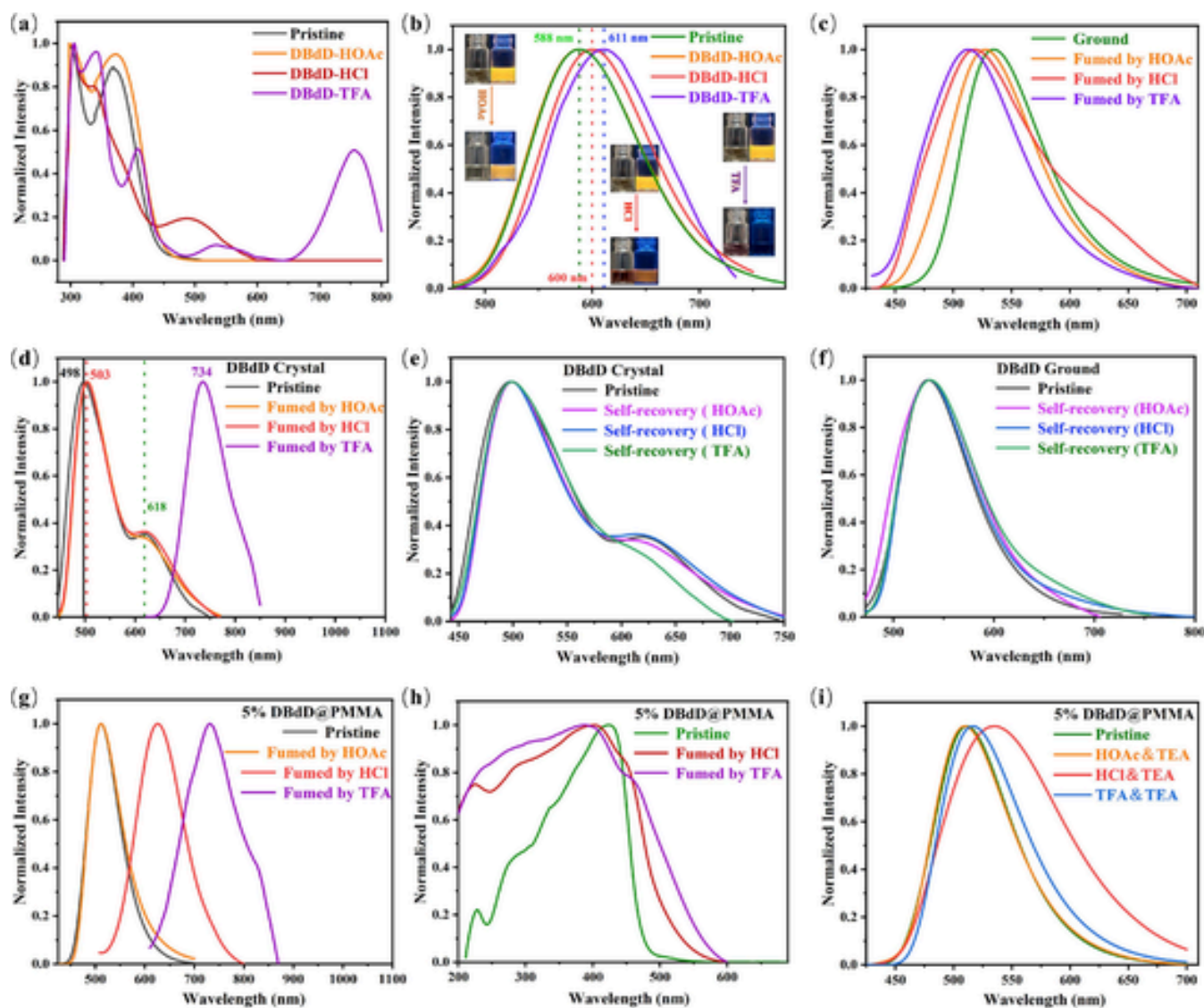


**Fig. 2.** (a) Normalized absorption and (b) fluorescence spectra of DBdD ( $\lambda_{\text{ex}} = 372$  nm) in neutral and acidic DCM solutions ( $10^{-5}$  M) (adding two drops HCl, HOAc, or TFA per 2 mL DCM solutions). (c) Normalized fluorescence spectra of ground and (d) crystal DBdD samples before/after HCl, HOAc, or TFA fuming ( $\lambda_{\text{ex}} = 400$  nm). (e) Normalized fluorescence spectra of crystal DBdD fumed by HOAc, HCl, and TFA after being placed in a natural environment for 1 h ( $\lambda_{\text{ex}} = 372$  nm). (f) Normalized fluorescence spectra of ground DBdD fumed by HOAc, HCl, and TFA after being placed in a natural environment for 1 h ( $\lambda_{\text{ex}} = 372$  nm). (g) Normalized fluorescence spectra of 5% DBdD@PMMA films by HOAc, HCl, and TFA fuming ( $\lambda_{\text{ex}} = 400$  nm). (h) Normalized absorption spectra of 5% DBdD@PMMA films by HCl, and TFA fuming. (i) Normalized fluorescence spectra of 5% DBdD@PMMA films by HCl, HOAc, or TFA fuming before TEA fumigation ( $\lambda_{\text{ex}} = 400$  nm).

and HOAc fumigation PMMA films due to the absence of the complex. Notably,  $\Phi_{\text{F}}$  of 5% DBdD@PMMA film was up to 0.75, which was much higher than that of crystals and ground DBdD, which was attributed to the excellent dispersion and non-radiative energy loss suppression effects of PMMA matrix, but HCl and TFA fumigation resulted in a decrease in  $\Phi_{\text{F}}$  to 0.41 and 0.13 respectively, which were consistent with the energy gap law. Absorption spectra indicated that 5% DBdD@PMMA films gave increasing absorption ranges (200–600 nm) after HCl and TFA fumigation, implying the increased molecular conjugation for DBdD in the ground state (Fig. 2h). The reversibility of acidochromism was investigated by Et<sub>3</sub>N fumigation (3 min), which showed that emission maxima of 5% DBdD@PMMA film could not back to 510 nm after Et<sub>3</sub>N fumigation, especially for PMMA film fumed by TFA (Fig. 2i), which might be due to the changing environmental polarity. Overall, crystals DBdD showed “switch-on” and irreversible mechanochromisms, which was beneficial for generating high contrast

stimuli-responsive fluorescence and serving as a permanent one-time information encryption. Ground DBdD presented reversible and morphology dependent mechanochromisms, which could be used for repeated information encryption. Taking advantages of different fluorescence responses to HCl, HOAc, and TFA, DBdD were expected to use as anti-counterfeiting and identification of different acids. To sum up, DBdD presented distinct fluorescence emissions in different acidic environments due to various solvent polarities and the formation of intermolecular complex, rather than protonation, while mechanochromism of crystals DBdD were attributed to the partial phase transition from crystalline state to amorphous state and reduced intermolecular interactions, leading to the increase of molecular motion and the quenching of triplet excitons.

### 2.3. Host-guest doping

Host guest doping had become an efficient method constructing long afterglow materials. Owing to rapid generation ability of triplet excitons, excellent crystallinity, and low melting point, OMeBP was used as host materials, whose purity was confirmed by HPLC (Fig. S18). Thereby a series of doping systems were constructed by melting, which were named as 0.01 % OMeBP/DBdD, 0.1 % OMeBP/DBdD, 1 % OMeBP/DBdD, and 10 % OMeBP/DBdD at the mass ratios of 10000:1, 1000:1, 100:1, and 10:1 between OMeBP and DBdD respectively (Fig. S6a). Switching on-off 365 nm UV lamp, 1 % OMeBP/DBdD showed the longest yellow-green afterglow and strongest delayed emission (Fig. S6b), with delay lifetimes of 566.45 ms and afterglow of 7 s (Fig. 3a and Fig. 3f). Surprisingly, both fluorescence and delay emission maxima of 1 % OMeBP/DBdD were 534 nm (Fig. 3b), and delay emission maxima maintained stable by changing delayed times (Fig. S6c), corresponding to CIE color coordinates of (0.37, 0.58) (Fig. S6d). Based on

the same delay and fluorescence emission maxima (Fig. 3b),  $\Delta E_{ST}$  of 1 % OMeBP/DBdD could be approximated as 0.00 eV, which made us doubted that the above delay emission of 1 % OMeBP/DBdD was not RTP but rather belonged to TADF. Temperature-variable delay spectra ( $\tau_d = 1$  ms) indicated that delay emission intensity of 1 % OMeBP/DBdD was increased by about six times with the increase of temperature from 77 K to 303 K, accompanied by blue shifts of emission maxima from 554 nm to 534 nm (Fig. 3c). It was widely known that low temperature could better suppress molecular rotation and vibration, resulting in blue shifts rather than red shifts of emission maxima, which was opposite to the above phenomenon. Therefore, decay emission of 1 % OMeBP/DBdD should mainly be TADF emission at room temperature (RT), but at 77 K it came from RTP of DBdD, which was confirmed by close emission maxima for 1 % OMeBP/DBdD (554 nm) and DBdD (556 nm) at 77 K (Fig. 3c and Fig. 3d). Furthermore, fluorescence and delayed spectra of 1 % OMeBP/DBdD were investigated at 303–323 K (Fig. S6e-g), indicating stable afterglow lifetimes, fluorescence and

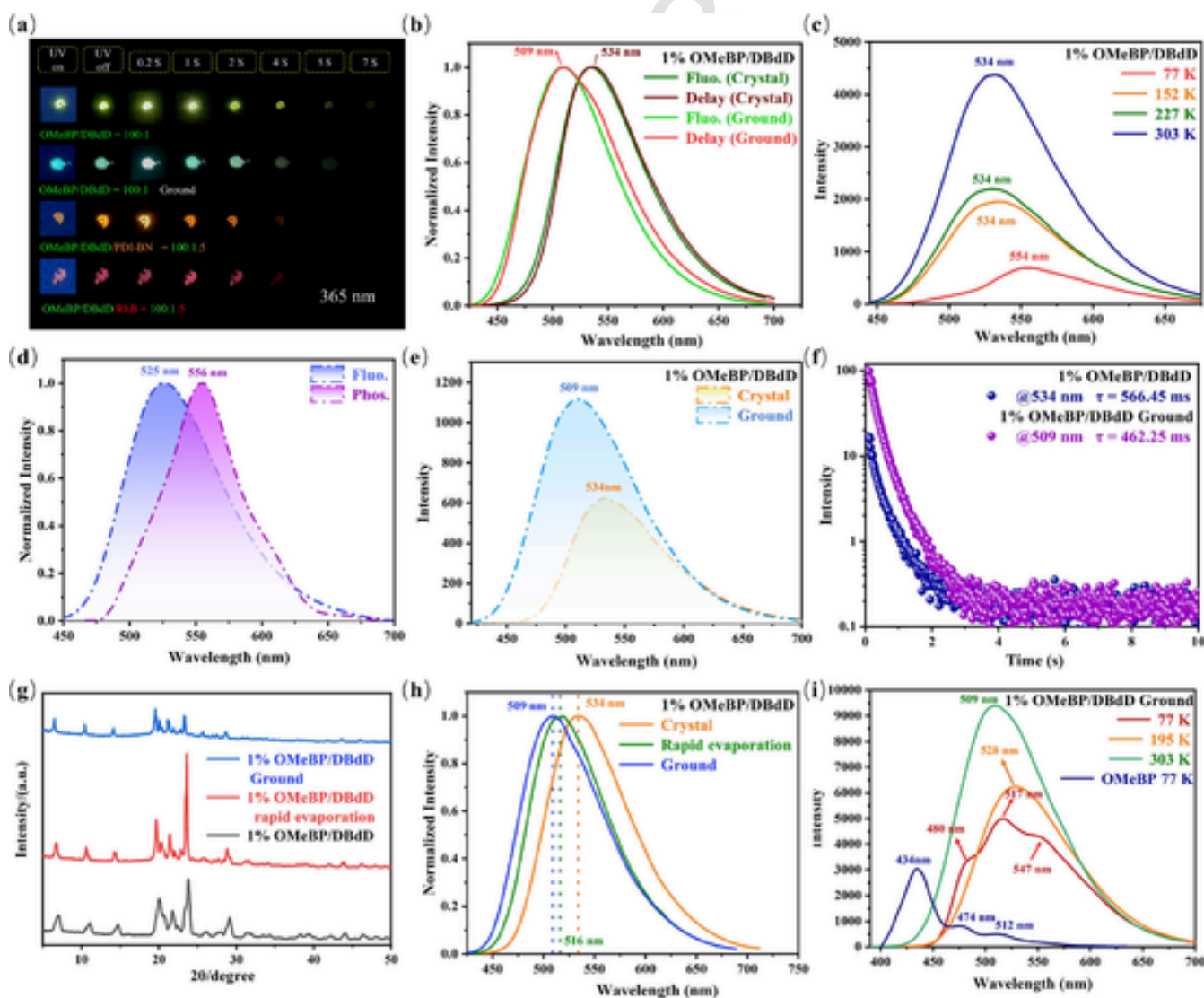


**Fig. 3.** (a) Photographs of before/after grinding 1 % OMeBP/DBdD, OMeBP/DBdD/PDI-BN = 100:1:5, and OMeBP/DBdD/RhB = 100:1:5 by turning on/off 365 nm UV lamp ( $\lambda_{ex} = 365$  nm). (b) Normalized fluorescence and delay spectra of before/after grinding ( $\lambda_{ex} = 365$  nm). (c) Temperature-variable delay spectra of before grinding ( $\lambda_{ex} = 365$  nm). (d) Normalized fluorescence ( $\lambda_{ex} = 372$  nm) and delay ( $\lambda_{ex} = 365$  nm) spectra of DBdD in THF ( $10^{-5}$  M) at 77 K. (e) Delay spectra of before/after grinding ( $\lambda_{ex} = 365$  nm). (f) Time-resolved decay curves of before/after grinding ( $\lambda_{ex} = 365$  nm). (g) Powder XRD patterns of in different solid states. (h) Normalized delay spectra of in different solid states ( $\lambda_{ex} = 365$  nm). (i) Temperature-variable delay spectra of after grinding ( $\lambda_{ex} = 365$  nm) and delay spectra of OMeBP at 77 K ( $\lambda_{ex} = 365$  nm).

TADF intensities, which was due to the fact that increasing temperature not only accelerated  $k_{\text{RISC}}$ , but also intensified molecular rotations and vibrations. Thermogravimetric analysis (TGA) of DBdD showed DBdD had excellent thermal stability, with thermal decomposition temperature ( $T_d$ ) of 400 °C (Fig. S7c). After soaking in water for 24 h, the afterglow lifetime of 1 % OMeBP/DBdD still lasted for 7 s, while its TADF intensity only showed a 5 % decrease (Fig. S7a-b).

Considering mechanochromism of DBdD, afterglow and delay spectra ( $\tau_d = 1$  ms) of ground 1 % OMeBP/DBdD were also examined. The results showed that delay emission maxima remained stable at different delay times (Fig. S7d), while ground 1 % OMeBP/DBdD presented attenuated delay intensity (Fig. 3e) and blue-shifted emission maxima from 534 nm to 509 nm (Fig. 3b), with a noticeable afterglow color transition from yellow to green, as well as the shortened delay and afterglow lifetimes from 566.45 ms and 7 s to 462.25 ms and 5 s (Fig. 3a and Fig. 3f). Furthermore, the absolute fluorescence ( $\Phi_f$ ) and delay quantum yields ( $\Phi_d$ ) of 1 % OMeBP/DBdD were 0.16 and 0.02 respectively at RT, but  $\Phi_f$  of ground 1 % OMeBP/DBdD dropped sharply to 0.04, accompanied by  $\Phi_d$  (0.05) of twice the pristine sample (Table S2). Generally, grinding increased oxygen exposure of triplet excitons and molecular motions, the grinding induced delay emission enhancement was rare. To understand the internal mechanism of mechanochromism, powder X-ray diffraction (XRD) analysis of 1 % OMeBP/DBdD was firstly investigated before/after grinding. Contrary to expectations, XRD signals of 1 % OMeBP/DBdD became sharper after grinding, display more ordered intermolecular stacking and arrangement, but 1 % OMeBP/DBdD presented the same diffraction peaks before/after grinding (Fig. 3g). Different from DBdD, the melting temperature of ground 1 % OMeBP/DBdD increased slightly (0.22 °C) compared with the pristine 1 % OMeBP/DBdD (Fig. S14c), implying reduced molecular motions and enhanced intermolecular interactions, which was consistent with XRD results. Based on the above test results, 1 % OMeBP/DBdD generally had the same intermolecular arrangement and stacking modes before/after grinding, while sharp diffraction signals should be due to stronger intermolecular interactions between host and guest molecules after grinding. In other words, the pristine 1 % OMeBP/DBdD samples contained a small amount of amorphous DBdD, while grinding reduced the content of amorphous DBdD in the above doping system. To tune the content of amorphous DBdD, 1 % OMeBP/DBdD was dissolved in DCM solution, and then dropped onto a glass plate for rapid evaporation. The results indicated that 1 % OMeBP/DBdD presented the same diffraction peaks by rapid solvent evaporation and grinding due to excellent crystallinity for OMeBP, but the former had wide diffraction XRD signals and red shifted decay emission maxima compared with the latter (Fig. 3g and Fig. 3h). Thereby, the internal mechanism of mechanochromism for 1 % OMeBP/DBdD were attributed to different contents of amorphous DBdD after grinding. Furthermore, ground 1 % OMeBP/DBdD also gave the same fluorescence and RTP emission maxima, then TADF emission characteristic was confirmed by temperature-variable delay spectra ( $\tau_d = 1$  ms) (Fig. 3i). Moreover, excitation spectra of emission maxima at 534 nm and 509 nm completely overlapped, demonstrating that delay emission came from the same excited state before/after grinding (Fig. 4c). Solid-state absorption spectra of OMeBP, DBdD, crystal and ground 1 % OMeBP/DBdD confirmed that no complex was formed due to the absence of new absorption peaks in doping systems of 1 % OMeBP/DBdD (Fig. 4d). At RT, crystal OMeBP gave a main fluorescence peak at 453 nm and two shoulder peaks at 420 and 480 nm, as well as a main RTP peak at 512 nm and two shoulder peaks at 446 and 555 nm (Fig. S7e). What was more, visible afterglow was not be perceived for crystal OMeBP at RT. Therefore, fluorescence and RTP of crystal OMeBP was excluded from long afterglow of 1 % OMeBP/DBdD due to mismatched emission maxima and spectra. In diluted THF solution at 77 K, phosphorescence emission maxima of DBdD were located at 556 nm (Fig. 3d), thereby single-molecule phosphorescence of DBdD was also elimi-

nated from long afterglow of 1 % OMeBP/DBdD. Most importantly, TADF emission maxima (534 nm) of 1 % OMeBP/DBdD before grinding basically matched with fluorescence emission maxima (536 nm) of ground DBdD, and both all exhibit sharp diffraction peaks, while TADF emission maxima (509 nm) of ground 1 % OMeBP/DBdD was close to fluorescence emission maxima (498 nm) of crystal DBdD, and with widened diffraction peaks. However, phosphorescence emission (618 nm) of DBdD was not found in ground 1 % OMeBP/DBdD, which should be due to the dispersal effect of OMeBP to DBdD. Therefore, long afterglow of 1 % OMeBP/DBdD before/after grinding was ascribed to singlet emission of similar to amorphous and crystalline DBdD respectively, while the energy transfer process from OMeBP to DBdD endowed 1 % OMeBP/DBdD with long TADF and afterglow lifetimes. Subsequently, the mechanochromism and TADF properties of OMeBP/DBdD were further investigated at different doping concentrations (Fig. S8-9). For 0.1 % OMeBP/DBdD, grinding led to shortened afterglow (Fig. S8a) and TADF lifetimes (Fig. S8c-d), as well as blue shifted fluorescence and delay emission maxima from 542 nm to 520 nm (Fig. S8b), accompanied by a noticeable afterglow color change from yellow to green (Fig. S8a). The TADF lifetime of 10 % OMeBP/DBdD also exhibited the same trend before/after grinding (Fig. S8f) (Fig. S9a), but with stable afterglow color and lifetime (Fig. S8a), as well as fluorescence and delay emission maxima (Fig. S8e), indicating the loss of mechanochromism at high doping concentration. Furthermore, the blue shifted emission maxima and the enhanced emission intensity (Fig. S9f) of 0.1 % OMeBP/DBdD and 10 % OMeBP/DBdD confirmed that the TADF characteristics of OMeBP/DBdD did not change at different doping concentrations based on the variable temperature delay spectra (Fig. S9b-e). To conduct an in-depth discussion on the differences in persistent luminescence lifetimes caused by different host-guest doping ratios, we tested the XRD patterns of 0.01 % OMeBP/DBdD, 0.1 % OMeBP/DBdD, 1 % OMeBP/DBdD, and 10 % OMeBP/DBdD (Fig. S14a). The results showed that the main XRD characteristic peaks of these samples were almost identical in position, with only varying degrees of sharpness. Among them, 1 % OMeBP/DBdD exhibited the best crystallinity, followed by 0.1 % OMeBP/DBdD, 10 % OMeBP/DBdD, and 0.01 % OMeBP/DBdD. This order was consistent with the sequence of persistent luminescence lifetimes from long to short. Furthermore, we measured the DSC curves of 0.1 % OMeBP/DBdD, 1 % OMeBP/DBdD, and 10 % OMeBP/DBdD (Fig. S14d), which indicated that the melting temperatures of these samples, from high to low, were 1 % OMeBP/DBdD (61.68 °C), 0.1 % OMeBP/DBdD (61.15 °C), and 10 % OMeBP/DBdD (60.00 °C). This suggested that 1 % OMeBP/DBdD had the strongest intermolecular interactions. In summary, different doping ratios affect the crystalline properties and intermolecular interactions of OMeBP/DBdD system, thereby leading to different persistent luminescence lifetimes. The stronger the crystallinity and intermolecular interactions, the longer the phosphorescence lifetime [53].

Red and near-infrared long afterglow materials have deep penetration and weak destruction to biological tissues, showing great potential in biosensing and bioimaging, but they are difficult to obtain due to the localized triplet emission characteristics and susceptibility to non-radiative quenching. With the help of FRET theory, some red and near-infrared materials had been reported one after another. Owing to the matching energy between TADF emission spectra of 1 % OMeBP/DBdD and absorption spectra of PDI-BN and Rhodamine B (RhB) (Fig. S10a), two doping systems named as OMeBP/DBdD/PDI-BN and OMeBP/DBdD/RhB were constructed at the mass ratio of 100:1:5. As expected, OMeBP/DBdD/PDI-BN and OMeBP/DBdD/RhB presented bright orange and red afterglows respectively (Fig. 3a), lasting over 4 s, with emission maxima of 590 nm and 646 nm, as well as decay lifetimes of 392.42 ms and 417.81 ms in turn (Fig. S10b-d), corresponding to energy transfer efficiency of 36 % and 38 % (Table S3) respectively, which illustrated that effective energy transfer occurred from singlet excitons of 1 % OMeBP/DBdD to singlet excitons of PDI-BN and RhB.

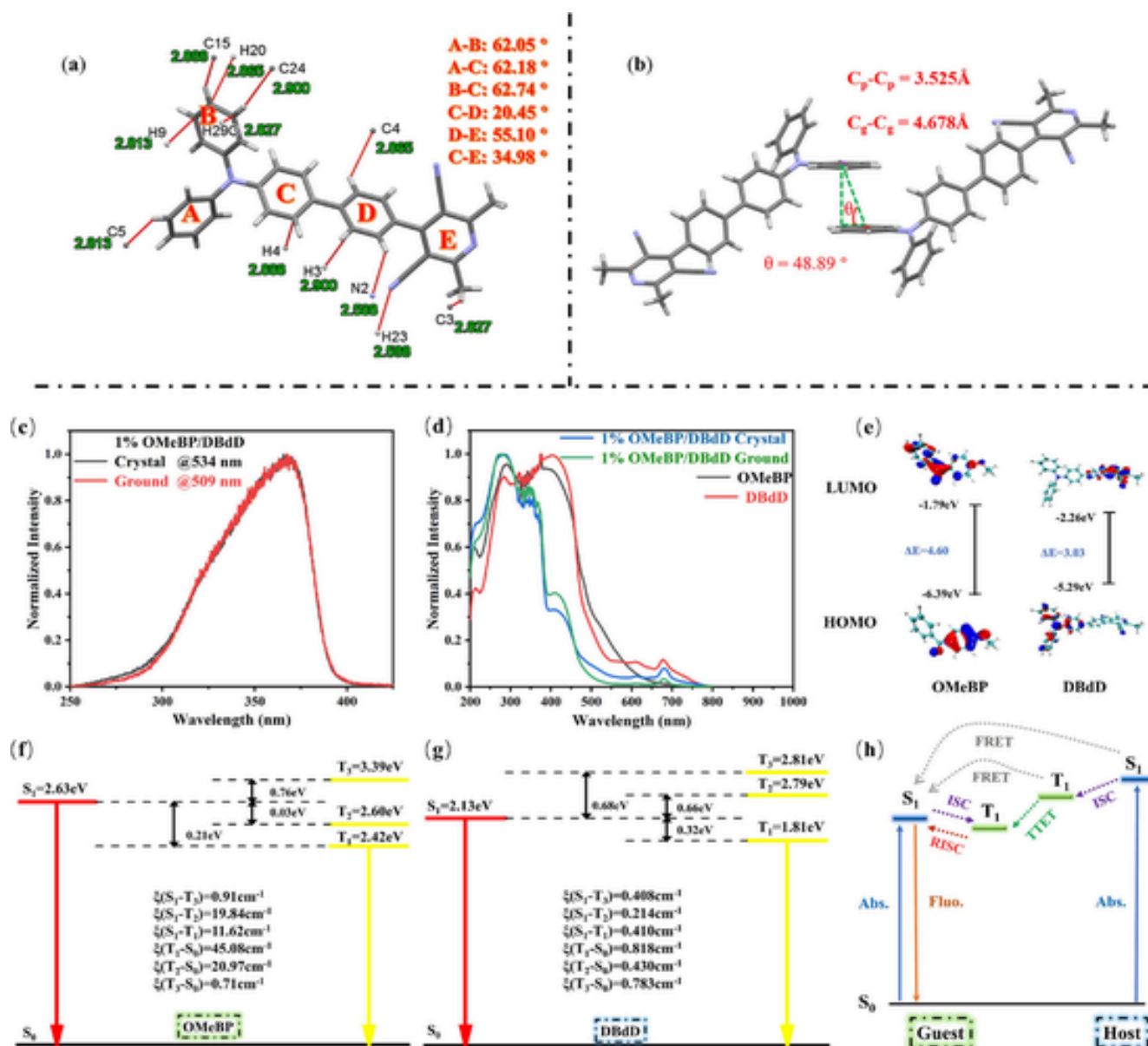


**Fig. 4.** (a) Molecular conformation and intermolecular weak interactions of crystal DBdD. (b) The intermolecular  $\pi$ - $\pi$  stacking of crystal DBdD. (c) Excitation spectra of 1% OMeBP/DBdD at TADF emission maxima before/after grinding. (d) Normalized absorption spectra of OMeBP and DBdD in solid state, as well as 1% OMeBP/DBdD before/after grinding. (e) HOMO and LUMO distributions of OMeBP and DBdD. (f) Energy levels and  $\xi$  of OMeBP and (g) DBdD. (h) Proposed photophysical processes in host-guest doping systems.

#### 2.4. Crystal analysis and theoretical calculations

To make clear mechanochromism and photophysical properties of crystals DBdD, single-crystal analysis was performed. Crystal DBdD (CCDC 2381983) was a triclinic system with the space group P-1 [ $a = 8.5908(6) \text{ \AA}$ ,  $b = 10.0025(6) \text{ \AA}$ , and  $c = 15.5230(12) \text{ \AA}$ ;  $\alpha = 82.936(4)^\circ$ ,  $\beta = 73.994(2)^\circ$ , and  $\gamma = 77.808(2)^\circ$ ]. DBdD showed twisted molecular conformation, with dihedral angles of 62.05°, 62.18°, 62.74°, 20.45°, and 55.10° for rings A-B, A-C, B-C, C-D, and D-E respectively (Fig. 4a). One DBdD molecule interacted with six surrounding molecules by C-H $\cdots$ C, C-H $\cdots$ N, and C-H $\cdots$  $\pi$  (Fig. S11a-c), but non radiative deactivation of triplet excitons caused by molecular motion and oxygen quenching could not be effectively suppressed, resulting in the absence of visible afterglow in the crystalline state. In a cell unit, there were two molecules adopting head-to-tail arrangement, without intermolecular

$\pi$ - $\pi$  stacking (Fig. S11d). By further expanding intermolecular interactions, intermolecular  $\pi$ - $\pi$  stacking were found between two adjacent TPA units, with plane-to-plane ( $C_p-C_p$ ) and centroid-to-centroid ( $C_g-C_g$ ) distances of 3.525 Å and 4.678 Å in sequence, corresponding to a pitch angle of 48.89° (Fig. 4b), which should be responsible for the emission peak at 618 nm.

The geometry optimizations of OMeBP and DBdD were performed at the B3LYP/def2-TZVP level using D4 dispersion correction, and all single-point calculations were performed at B3LYP/def2-TZVP level. Then the highest occupied molecular orbitals (HOMO) and the lowest unoccupied molecular orbitals (LUMO) distribution, energy levels, and spin orbit coupling constants ( $\xi$ ) between singlet and triplet states were obtained. OMeBP and DBdD exhibited a separated HOMO and LUMO electron cloud density distribution, indicating strong ICT effect, especially for DBdD (Fig. 4e). Moreover, HOMO and LUMO energy levels of

OMeBP were embedded between HOMO and LUMO energy levels of DBdD, contributing to boosting energy transfer from OMeBP to DBdD. Furthermore, OMeBP (0.21 eV) and DBdD (0.32 eV) had suitable  $\Delta E_{ST}$  for ISC (Fig. 4f and Fig. 4g). Notably,  $\xi(S_1 \rightarrow T_1)$  and  $\xi(T_1 \rightarrow S_0)$  of OMeBP were up to 11.62  $\text{cm}^{-1}$  and 45.08  $\text{cm}^{-1}$  respectively, thereby OMeBP was suitable for used as an efficient triplet exciton pump, but such high  $\xi(T_1 \rightarrow S_0)$  easily led to the fast phosphorescence radiation rate and short afterglow lifetime, which was consistent with the imperceptible afterglow of crystal OMeBP to the naked eyes at RT. By contrast,  $\xi(S_1 \rightarrow T_1)$  and  $\xi(T_1 \rightarrow S_0)$  of DBdD were 0.41  $\text{cm}^{-1}$  and 0.82  $\text{cm}^{-1}$  in sequence, showing that DBdD had phosphorescence nature, but small  $\xi(S_1 \rightarrow T_1)$  and  $\xi(T_1 \rightarrow S_0)$  resulted in DBdD exhibiting weak RTP and short afterglow lifetime (0.7 s) even in rigid polyvinyl alcohol (PVA) films. Based on the natural transition orbitals (NTOs) calculation, DBdD showed  $S_1$  and  $T_1$  states with predominantly  $^1(n, \pi)$  and  $^3(\pi, \pi)$  characters in sequence, which was beneficial to boosting ISC between  $S_1$  and  $T_1$  states and reducing the phosphorescent radiation rate, leading to long afterglow lifetimes (Fig. S15). Consistent with the calculation results, DBdD presented yellow afterglow in glassy THF, lasting for 3 s. However, crystals DBdD could not emit visible afterglow in air and anaerobic environments (Fig. S14e), which was attributed to the deactivation of triplet excitons caused by molecular motions. Of note, fluorescence and RTP maxima of 1 % DBdD@PVA film were located at 498 nm and 556 nm with 64.85 ms lifetimes (Fig. S12d-e), corresponding to  $\Delta E_{ST}$  of 0.27 eV. Meanwhile, 1 % DBdD@PVA film presented stable phosphorescence emission maxima at various temperature stages and continuously decreasing RTP intensity as the temperature increased (Fig. S12c). Therefore, 1 % DBdD@PVA film showed RTP rather than TADF.

Furthermore, we tested the UV-Vis absorption spectrum of DBdD in THF solution and the solid-state fluorescence and phosphorescence spectra of OMeBP (Fig. S13a-b). The results showed a small number of overlapping areas in these spectra, suggesting weak FRET between DBdD and OMeBP. Based on theoretical calculations and experimental test results, the  $T_1$  state energy levels of OMeBP were 2.42 eV and 2.76 eV (Fig. 4f and Fig. S7e), while those of DBdD are 1.81 eV and 2.23 eV (Fig. 3d and Fig. 4g), satisfying the triplet-triplet energy transfer process (TTET) from OMeBP to DBdD. The XRD signals of ground 1 % OMeBP/DBdD became sharper, indicating a more ordered intermolecular arrangement, which was beneficial for shortening intermolecular distance and improving the TTET process [52], leading to doubled TADF quantum yield for 1 % OMeBP/DBdD before (0.02) and after grinding (0.05) (Table S2). When selectively excited at 450 nm (Fig. S13c), the delayed spectrum of 1 % OMeBP/DBdD showed a significant red shift compared to that of solid-state OMeBP (Fig. S13d), further confirming the TTET process. Thereby, photophysical processes of 1 % OMeBP/DBdD were outlined (Fig. 4h). When 1 % OMeBP/DBdD was irradiated by a 365 nm UV lamp, OMeBP and DBdD electrons transitioned to the lowest excited singlet states of host ( $S_{H1}$ ) and guest ( $S_{G1}$ ) from the ground states of the host ( $S_{H0}$ ) and guest ( $S_{G0}$ ), then transferred to their respective excited triplet states  $T_{H1}$  and  $T_{G1}$  via ISC of ( $S_1 \rightarrow T_1$ ) and rapid internal conversion. Notably, the vast majority of triplet excitons came from OMeBP due to the low doping concentration of DBdD. The abundant excitons at  $T_{H1}$  transferred to  $T_{G1}$  by TTET and FRET processes. Finally, the excitons at  $T_{G1}$  transferred to  $S_{G1}$  via rapid reverse intersystem crossing (RISC), and then back to  $S_{G0}$ , thereby emitting bright TADF. Of note, theoretical calculations ignored intermolecular interactions between OMeBP and DBdD, resulting in the increased  $\Delta E_{ST}$  for DBdD. In THF solution at 77 K, fluorescence and phosphorescence emission maxima of DBdD were 525 nm and 556 nm respectively, corresponding to  $S_1$  of 2.36 eV and  $T_1$  state energy levels of 2.23 eV in turn, as well as  $\Delta E_{ST}$  of 0.12 eV. In 1 % OMeBP/DBdD, fluorescence and decay emission maxima of DBdD were 534 nm, 554 nm, 509 nm, and 547 nm before/after grinding respectively, corresponding to  $S_1$  state energy levels of 2.32 eV and 2.44 eV,  $T_1$  state energy levels of

2.24 eV and 2.27 eV, as well as  $\Delta E_{ST}$  of 0.08 eV and 0.17 eV in sequence. The small  $\Delta E_{ST}$  led to rapid RISC, endowing DBdD with TADF emission capability at RT in 1 % OMeBP/DBdD. Obviously, DBdD displayed host-dependent luminescent characteristics. Under 365 nm UV lamp radiation, DBdD itself also could yield weak TADF emission by ISC and RISC due to the inhibition of molecular motion and oxygen diffusion in 1 % OMeBP/DBdD. Overall, DBdD itself has the characteristics of phosphorescence and long afterglow, but the molecular motions cause invisible afterglow for crystals DBdD. The long afterglow observed in 1 % OMeBP/DBdD was attributed to multiple energy transfer processes including FRET, TTET, and reverse intersystem crossing, extending the afterglow lifetime of 1 % OMeBP/DBdD.

### 2.5. Application

Based on different afterglow lifetimes of OMeBP/DBdD at different doping mass ratios, a set of numbers "88" was constructed by melting and using molds (Fig. 5a). By switching on/off a 365 nm UV lamp, the number "88" sequentially became "28", "25", and "2". Assuming that "88", "28", "25", and "2" corresponded to the letter "r", "e", "a", and "l" in turn, and the encrypted word "real" could be obtained by decrypting the initial numbers "88" over time. Subsequently, a "flower" pattern with leaves were drawn by using DCM solution of 1 % OMeBP/DBdD, OMeBP/DBdD/RhB, and OMeBP/DBdD/PDI-BN on a printing paper (Fig. 5b). In sunlight, the pattern showed red inner and orange yellow outer petals, as well as green leaves. Under 365 nm UV radiation, green leaves were clearly visible, while the flower was difficult to distinguish. Switching off the 365 nm lamp, the flower began to appear, which became clearer within 1–2 s after turning off the UV light due to the delay of FRET. After 4 s, only the green leaves remained due to shorter afterglow lifetimes for OMeBP/DBdD/RhB, and OMeBP/DBdD/PDI-BN than 1 % OMeBP/DBdD. DBdD of 5 mg was dispersed into n-hexane (5 mL) under ultrasound (2 min), and then a common filter paper was immersed in the above suspension. After 2 min, the filter paper was taken out and dried at RT for 2 h. Under 365 nm UV radiation, the filter paper presented blue fluorescence. When the word "Myself" was written on it by a inkless pen, the corresponding information encryption was completed. When 365 nm UV were turned on, the bright green word "Myself" became particularly prominent under the light-yellow background (Fig. 5c). Subsequently, the filter paper was exposed to an atmosphere of  $\text{CF}_3\text{COOH}$  for information hiding. By  $\text{Et}_3\text{N}$  fuming, the information was decrypted again, presenting the green word "Myself".

### 3. Conclusions

In summary, the dual-state fluorescence emission was achieved by furnishing DBdD with planar diphenyl core and twisted TPA and MCP units, affording the maximum  $\Phi_{RF}$  of 0.50 and 0.38 in dilution toluene and aggregated state respectively. RTP (618 nm) and fluorescence (498 nm) emission were simultaneously observed in the pristine crystals DBdD, while grinding triggered "switch-on" type mechanochromism due to the phase transition from crystalline-to-partial amorphous state causing intensified molecular motions. Moreover, DBdD presented morphology dependent mechanochromism by repeated grinding and heating/DCM fuming. ICT and host-guest doping contribute to long TADF afterglow and mechanochromism with lifetime dimension, whose TADF and afterglow lifetimes were 566.45 ms, 7 s and 462.25 ms, 5 s respectively before/after grinding. Of note, such long TADF lifetime and afterglow were rarely reported before this study. Orange (595 nm) and red (650 nm) long afterglows were further developed by three components doping and FRET mechanism, with decay lifetimes of 392.42 ms and 417.81 ms respectively, as well as afterglow over 4 s. By the formation of different complexes, DBdD could respond selectively and distinguish  $\text{CH}_3\text{COOH}$ , HCl, and  $\text{CF}_3\text{COOH}$  in DCM solution, solid state, and PMMA films. Based on acidochromism,

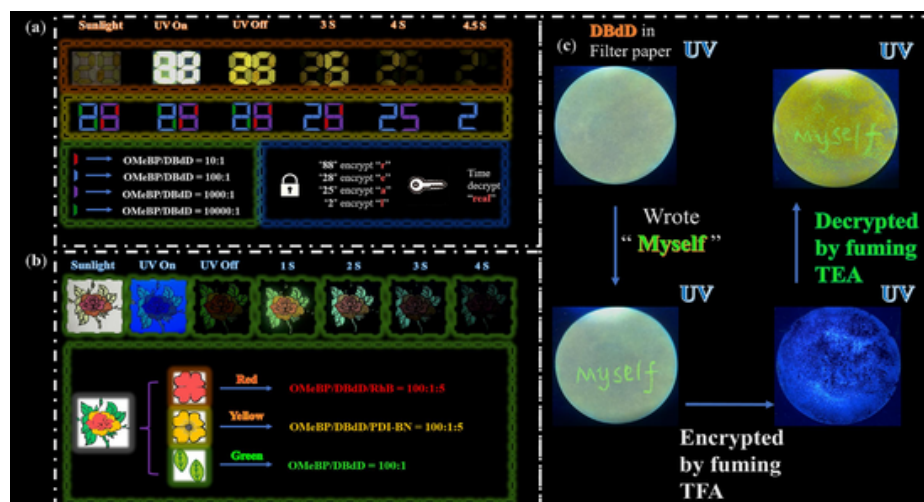


**Fig. 5.** (a) Data encryption by using 0.01 % OMeBP/DBdD, 0.1 % OMeBP/DBdD, 1 % OMeBP/DBdD, and 10 % OMeBP/DBdD ( $\lambda_{\text{ex}} = 365 \text{ nm}$ ). (b) “Flower” pattern was drawn by using DCM solutions of 1 % OMeBP/DBdD, OMeBP/DBdD/PDI-BN = 100:1:5 and OMeBP/DBdD/RhB = 100:1:5 respectively ( $\lambda_{\text{ex}} = 365 \text{ nm}$ ). (c) Data encryption and decryption via mechanochromism and acidochromism of DBdD ( $\lambda_{\text{ex}} = 365 \text{ nm}$ ).

different afterglow lifetimes, and multi-color long afterglow, the advanced information encryption and anti-counterfeiting were successfully constructed. This work not only provided a multifunctional luminogen for developing dual-state emission, acidochromism and simple recognition of volatile HCl,  $\text{CF}_3\text{COOH}$ , and  $\text{CH}_3\text{COOH}$ , “switch-on” type and morphology dependent mechanochromism, TADF type and multi-color long afterglow, but also provided valuable insights into the mechanisms governing scarce “switch-on” type mechanochromism and TADF type long afterglow.

#### CRediT authorship contribution statement

**Chao Yang:** Writing – original draft, Validation, Methodology, Data curation. **Meiling Pan:** Writing – original draft, Software, Data curation. **Lei Ma:** Writing – review & editing, Supervision, Software. **Yongtao Wang:** Writing – review & editing, Project administration, Funding acquisition, Conceptualization.

#### Declaration of competing interest

The authors declare that they have no known competing financial interests or personal relationships that could have appeared to influence the work reported in this paper.

#### Acknowledgments

This work was supported by the Guangxi Natural Science Foundation (Grant No. 2024GXNSFAA999457 and 2020GXNSFAA159147), the National Natural Science Foundation of China (Grant No. 21766030).

#### Data availability

The authors do not have permission to share data.

#### Appendix A. Supplementary data

Supplementary data to this article can be found online at <https://doi.org/10.1016/j.cej.2025.163205>.

#### References

- [1] Y.-J. Lin, M. Horie, Dithienylethene-containing cyclic and linear conjugated molecules: synthesis, photochromism, and photoluminescence, *Dyes Pigm.* 195 (2021) 109700.
- [2] E. Kościeln, E. Gondek, B. Jarosz, A. Danel, J. Nizioł, A.V. Kityk, Photoluminescence of 1-phenyl,3-methyl pyrazoloquinoline derivatives, *Spectrochim. Acta, Part A* 72 (2009) 582–590.
- [3] J. Yang, Z. Ren, B. Chen, M. Fang, Z. Zhao, X.-Z. Tang, Q. Peng, Z. Li, Three polymorphs of one luminogen: how the molecular packing affects the RTP and AIE properties, *J. Mater. Chem. C* 5 (2017) 9242–9246.
- [4] J. Ma, Y. Zhou, H. Gao, F. Zhu, G. Liang, Full-type photoluminescence from a single organic molecule for multi-signal temperature sensing, *Mater. Chem. Front.* 5 (2021) 2261–2270.
- [5] C. Ma, X. Zhang, Y. Yang, Z. Ma, L. Yang, Y. Wu, H. Liu, X. Jia, Y. Wei, Halogen effect on mechanofluorochromic properties of alkyl phenothiazinyl phenylacrylonitrile derivatives, *Dyes Pigm.* 129 (2016) 141–148.
- [6] J. Li, W.-C. Chen, H. Liu, Z. Chen, D. Chai, C.-S. Lee, C. Yang, Double-twist pyridine–carbonitrile derivatives yielding excellent thermally activated delayed fluorescence emitters for high-performance OLEDs, *J. Mater. Chem. C* 8 (2020) 602–606.
- [7] A. Bhadke, S. Lambud, Z.A. Siddiqui, A. Bommera, N. Sekar, S. More, Dual state emissive pyrene-fused benzopyrazoacenes and their solvatochromic behaviour, *J. Mol. Struct.* 1314 (2024) 138796.
- [8] S.K. Patra, R. Manivannan, Y.-A. Son, Multicolor emissive organic material to display aggregation caused red shift with dual state emission, and application towards rewritable data storage, *Spectrochim. Acta, Part A* 444 (2023) 114945.
- [9] Z. Meng, Y. Li, K. Liao, Y. Sun, W. Zhang, B. Song, X. Zhu, X.-Q. Hao, Dual state emissive tridentate imidazopyridines with applications in acidochromism, metal ions detection, data encryption, and bioimaging, *Dyes Pigm.* 222 (2024) 111882.
- [10] H. Wu, Z. Chen, W. Chi, A.K. Bindra, L. Gu, C. Qian, B. Wu, B. Yue, G. Liu, G. Yang, L. Zhu, Y. Zhao, Structural engineering of luminogens with high emission efficiency both in solution and in the solid state, *Angew. Chem., Int. Ed.* 131 (2019) 11541–11545.
- [11] Y. Yu, H. Xing, Z. Zhou, J. Liu, H.H.Y. Sung, I.D. Williams, J.E. Halpert, Z. Zhao, B.Z. Tang, How do molecular interactions affect fluorescence behavior of AIEgens in solution and aggregate states, *Sci. China: Chem.* 65 (2021) 135–144.
- [12] P. Han, G. Zhang, J. Wang, Y. Yao, Y. Qiu, H. Xu, A. Qin, B.Z. Tang, Highly emissive luminogens in both solution and aggregate states, *CCS Chem.* 5 (2023) 1686–1696.
- [13] A. Cheng, Y. Jiang, H. Su, B. Zhang, J. Jiang, T. Wang, Y. Luo, G. Zhang, Origin of red-shifted phosphorescence from triphenylamines: triplet excimer or impurity, *Angew. Chem., Int. Ed.* 61 (2022) e202206366.
- [14] J. Guo, Y. Zhao, L. Ma, Y. Wang, Ultra-long room temperature phosphorescence, intrinsic mechanisms and application based on host-guest doping systems, *Chin. J. Struct. Chem.* 43 (2024) 100335.
- [15] Y. Pan, J. Li, X. Wang, Y. Sun, J. Li, B. Wang, K. Zhang, Highly efficient TADF-type organic afterglow of long emission wavelengths, *Adv. Funct. Mater.* 32 (2021) 2110207.
- [16] L. Shi, J. Liu, L. Ma, Y. Wang, The dual-band emission with long-lived thermally activated delayed fluorescence and room temperature phosphorescence by trace ingredient incorporation, *Chem. Eng. J.* 493 (2024) 152492.
- [17] L. Ai, W. Xiang, J. Xiao, H. Liu, J. Yu, L. Zhang, X. Wu, X. Qu, S. Lu, Tailored fabrication of full-color ultrastable room-temperature phosphorescence carbon

- dots composites with unexpected thermally activated delayed fluorescence, *Adv. Mater.* 36 (2024) 2401220.
- [18] W. Li, Z. Li, C. Si, M.Y. Wong, K. Jinnai, A.K. Gupta, R. Kabe, C. Adachi, W. Huang, E. Zysman-Colman, I.D.W. Samuel, Organic long-persistent luminescence from a thermally activated delayed fluorescence compound, *Adv. Mater.* 32 (2020) 2003911.
- [19] S. Zhang, G. Liu, J. Chen, Y. Zhang, Q. Sun, S. Xue, W. Yang, Unexpected emission behaviors of rhodamine derivatives in PVA after UV–green light excitation, *Adv. Opt. Mater.* 11 (2023) 2301147.
- [20] K. Zhang, N. Dan, D.-D. Ren, R.-Y. Zhang, X. Lu, Y.-P. Wu, L.-L. Zhang, H.-R. Fu, D.-S. Li, A small D-A molecule with highly heat-resisting room temperature phosphorescence for white emission and anti-counterfeiting, *Chin. J. Struct. Chem.* 43 (2024) 100244.
- [21] G. Wang, X. Chen, Y. Zeng, X. Li, X. Wang, K. Zhang, Dual-mechanism design strategy for high-efficiency and long-lived organic afterglow materials, *J. Am. Chem. Soc.* 146 (2024) 24871–24883.
- [22] S. Shao, J. Hu, X. Wang, L. Wang, X. Jing, F. Wang, Blue thermally activated delayed fluorescence polymers with nonconjugated backbone and through-space charge transfer effect, *J. Am. Chem. Soc.* 139 (2017) 17739–17742.
- [23] C. Shi, D. Liu, J. Li, Z. He, K. Song, B. Liu, Q. Wu, M. Xu, Tert-butyltriazine-diphenylaminocarbazole based TADF materials:  $\pi$ -bridge modification for enhanced KRISC and efficiency stability, *Dyes Pigm.* 204 (2022) 110430.
- [24] Y. Wang, X. Qi, Z. Ye, Y. Yan, Q. Chen, Y. Yang, D. Gao, J. Zhao, J. Li, Single-component white afterglow from dual emission based on carbazole-pyrimidine-benzene derivatives, *Dyes Pigm.* 232 (2025) 112486.
- [25] X. Wang, Y. Sun, G. Wang, J. Li, X. Li, K. Zhang, TADF-type organic afterglow, *Angew. Chem., Int. Ed.* 133 (2021) 17275–17284.
- [26] Y. Wang, M. Gao, J. Ren, J. Liang, Y. Zhao, M. Fang, J. Yang, Z. Li, Exciplex-induced TADF, persistent RTP and ML in a host–guest doping system, *Mater. Chem. Front.* 7 (2023) 1093–1099.
- [27] X. Li, S. Shen, C. Zhang, M. Liu, J. Lu, L. Zhu, Small-molecule based thermally activated delayed fluorescence materials with dual-emission characteristics, *Sci. China: Chem.* 64 (2021) 534–546.
- [28] Y. Hong, Y. Zhao, L. Ma, Y. Wang, Tuning triplet excitons and dynamic afterglow based on host-guest doping, *Spectrochim. Acta, Part A* 324 (2025) 124955.
- [29] K. Chen, Y. Jiang, Y. Zhu, Y. Lei, W. Dai, M. Liu, Z. Cai, H. Wu, X. Huang, Y. Dong, Host to regulate the  $T_1$ - $S_1$  and  $T_1$ - $S_0$  processes of guest excitons in doped systems to control the TADF and RTP emissions, *J. Mater. Chem. C* 10 (2022) 11607–11613.
- [30] Y. Sun, L. Wu, L. Zhu, G.V. Baryshnikov, F. Zhang, X. Li, Recent advances in thermally activated delayed fluorescence-based organic afterglow materials, *Small Methods* 2400982 (2024).
- [31] X. Chen, G. Wang, J. Li, X. Chen, X. Zhao, Y. Zeng, Y. Su, K. Zhang, Difluoroboron  $\beta$ -diketonate systems: large transformation of photophysical mechanism induced by tiny structural modification or isomerization, *Adv. Opt. Mater.* 12 (2023) 2301619.
- [32] J. Zhang, J. Li, X. Li, S. Yuan, Y. Sun, Y. Zou, Y. Pan, K. Zhang, Boosting organic afterglow efficiency via triplet–triplet annihilation and thermally-activated delayed fluorescence, *J. Mater. Chem. C* 10 (2022) 4795–4804.
- [33] S. Hirata, M. Vacha, White afterglow room-temperature emission from an isolated single aromatic unit under ambient condition, *Adv. Opt. Mater.* 5 (2017) 1600996.
- [34] Y. Liu, D. Cheng, B. Wang, J. Yang, Y. Hao, J. Tan, Q. Li, S. Qu, Carbon dots-inked paper with single/two-photon excited dual-mode thermochromic afterglow for advanced dynamic information encryption, *Adv. Mater.* 36 (2024) 2403775.
- [35] R. Misra, R. Gavale, S.K. Pandit, Room temperature phosphorescence driven by mechanochromism, *Chem. Asian J.* (2025) e202401893.
- [36] C. Zhang, L. Lou, Y. Li, C. Li, D. Wang, H. Cao, W. He, Z. Yang, Organic room temperature phosphorescence enhancement by grinding and adding water for humidity detection and anti-counterfeiting printing, *New J. Chem.* 47 (2023) 15219–15225.
- [37] Y. Tani, M. Terasaki, M. Komura, T. Ogawa, Room-temperature phosphorescence-to-phosphorescence mechanochromism of a metal-free organic 1, 2-diketone, *J. Mater. Chem. C* 7 (2019) 11926–11931.
- [38] L. Huang, X. Wen, J. Liu, M. Chen, Z. Ma, X. Jia, An AIE molecule featuring changeable triplet emission between phosphorescence and delayed fluorescence by an external force, *Mater. Chem. Front.* 3 (2019) 2151–2156.
- [39] P. Pattanayak, A. Nandi, S.K. Seth, P. Purkayastha, Heavy-element-free triplet accessibility in pyrene-core compounds at room temperature by microcrystal engineering, *J. Mater. Chem. C* 11 (2023) 11252–11261.
- [40] J. Ren, Y. Wang, Y. Tian, Z. Liu, X. Xiao, J. Yang, M. Fang, Z. Li, Force-induced turn-on persistent room-temperature phosphorescence in purely organic luminogen, *Angew. Chem., Int. Ed.* 60 (2021) 12335–12340.
- [41] Y. Zhou, J. Song, Y. Hu, J. Cao, Y. Fu, X. Ma, Stimuli-responsive room-temperature phosphorescence regulation based on molecular packing mode conversion, *Dyes Pigm.* 215 (2023) 111272.
- [42] J.-F. Cheng, Z.-H. Pan, K. Zhang, Y. Zhao, C.-K. Wang, L. Ding, M.-K. Fung, J. Fan, Interrupted intramolecular donor-acceptor interaction compensated by strong through-space electronic coupling for highly efficient near-infrared TADF with emission over 800 nm, *Chem. Eng. J.* 430 (2022) 132744.
- [43] Z. Zhao, T. Zhu, A. Li, Q. Zhang, W. Zhang Yuan, Highly efficient red/near-infrared phosphorescence from doped crystals, *Angew. Chem., Int. Ed.* (2024) e202412967.
- [44] Y. Zhang, L. Chen, B. Liu, S. Yu, Y. Yang, X. Liu, Multicolor afterglow carbon dots: luminescence regulation, preparation, and application, *Adv. Funct. Mater.* 34 (2024) 2315366.
- [45] K. Chen, Y. Xiong, D. Wang, Y. Pan, Z. Zhao, D. Wang, B.Z. Tang, A facile strategy for achieving polymeric afterglow materials with wide color-tunability and persistent near-infrared luminescence, *Adv. Funct. Mater.* 34 (2023) 2312883.
- [46] F. Lin, H. Wang, Y. Cao, R. Yu, G. Liang, H. Huang, Y. Mu, Z. Yang, Z. Chi, Stepwise energy transfer: near-infrared persistent luminescence from doped polymeric systems, *Adv. Mater.* 34 (2022) 2108333.
- [47] Z. Ma, Y. Ji, Z. Wang, G. Kuang, X. Jia, Mechanically controlled FRET to achieve an independent three color switch, *J. Mater. Chem. C* 4 (2016) 10914–10918.
- [48] J. Wang, Y. Zhang, Z.-P. Yu, H. Huang, L. Chen, X. Zhu, J. Zhang, L. Wang, J. Yu, H. Zhou, Diversified photo-energy conversion based on single-molecule FRET to realize enhanced phototheranostics, *Mater. Chem. Front.* 5 (2021) 8229–8237.
- [49] P.W. McDonald, J. Xu, D.R. Lonsdale, I. Jones, B. Poggi, R.P. Cox, S. Aloise, A.D. Scully, C. Allain, L. Bodelot, S.A. Moggach, T.D.M. Bell, R. Métivier, S.G.B. Furness, L. Goerigk, C. Ritchie, Fluorescence modulation of pyridinium betaines: a mechanofluorochromic investigation, *J. Mater. Chem. C* 12 (2024) 19371–19385.
- [50] Y. Chen, A. Li, X. Li, L. Tu, Y. Xie, S. Xu, Z. Li, Multi-stimuli-responsive amphiphilic pyridinium salt and its application in the visualization of level 3 details in latent fingerprints, *Adv. Mater.* 35 (2023) 2211917.
- [51] Y. Xie, Y. Pan, F. Xiao, Y. Lei, Y. Zhou, M. Liu, W. Gao, X. Huang, H. Wu, Synthesis, crystal structures and solid-state acidochromism of multiaryl-substituted pyridine derivatives with aggregation-induced emission property, *Dyes Pigm.* 188 (2021) 109217.
- [52] J. Li, S. Hao, M. Li, Y. Chen, H. Li, S. Wu, S. Yang, L. Dang, S.J. Su, M.D. Li, Triplet energy gap-regulated room temperature phosphorescence in Host–Guest doped systems, *Angew. Chem., Int. Ed.* 64 (2024) e202417426.
- [53] W. Xie, W. Huang, J. Li, Z. He, G. Huang, B.S. Li, B.Z. Tang, Anti-Kasha triplet energy transfer and excitation wavelength dependent persistent luminescence from host-guest doping systems, *Nat. Commun.* 14 (2023) 8098.